





Calibration of reactive burn and Jones-Wilkins-Lee parameters for simulations of a detonation-driven flow experiment with uncertainty quantification

Joshua Garno , Frederick Ouellet , Sangjune Bae, Thomas L. Jackson, Nam-Ho Kim, Raphael Haftka, Kyle T. Hughes , and S. Balachandar 

Department of Mechanical and Aerospace Engineering, University of Florida, Gainesville, Florida 32611, USA



(Received 6 June 2020; accepted 16 November 2020; published 14 December 2020)

Uncertainties in the explosive-specific parameters of the Jones-Wilkins-Lee (JWL) equation of state (EOS) are carefully considered in hydrodynamic simulations of an explosive experiment to minimize the error in the flow prediction. Experimental data of the leading shock position in the transverse direction over time serves as the prediction metric for quantifying simulation prediction error. The uncertainty quantification technique, global sensitivity analysis, is utilized to determine the JWL parameters to which the transverse shock propagation is most sensitive. A polynomial response surface (PRS) is constructed in the space of the most influential JWL parameters, and the point of minimum error between the experimental data and the PRS yields calibrated JWL parameters for the experimental flow. The simulation results following the parameter calibration show good agreement with the experimental data. It was found that two significant parameters, the heat release per unit mass of reactant Q and JWL model exponent R_1 are strongly related, which makes it difficult to identify accurate values.

DOI: [10.1103/PhysRevFluids.5.123201](https://doi.org/10.1103/PhysRevFluids.5.123201)

I. INTRODUCTION

The hydrodynamic modeling of high explosives (HEs) during and after the detonation process is an ongoing topic of interest for munitions and mining applications. At the core of the modeling process is an equation of state (EOS), which relates the thermodynamic state variables of a material to a given set of physical conditions. Often, the physical conditions are given by the density, pressure, or temperature of the material. For example, the state variables of ambient air at standard temperature and pressure (STP) may be related by the well-known ideal gas law (see Sec. IV B 1). Such a model may be validated with common measurement techniques using widely available apparatuses. Conversely, the extreme pressures [$O(10$ GPa)], temperatures [$O(1000$ K)], and rapid time scales [$O(10$ ns)] associated with detonation events introduce challenges for equation-of-state development.

A defining property of high explosives is the detonation velocity, or the speed at which the reaction front propagates through the material after having reached a steady state. This quantity is dependent on the composition, geometry, and confinement associated with the reacting material [1]. For HMX-based explosives, this speed is reported to be in excess of 9 km/s [2]. Further, analysis on the expansion of trailing detonation products provides key information about the relationship between energy release and volumetric expansion of the reacted explosive material. These sources of information may be used to derive the material specific parameters of the widely used, empirically based Jones-Wilkins-Lee (JWL) EOS [3]. Developed at Lawrence Livermore National Laboratory

(LLNL), the primary method of characterizing the detonation velocity and adiabatic expansion of detonation products of a given explosive is the cylinder test [3,4]. The general experimental setup for the cylinder test consists of an electrically grounded copper tube filled with explosive material. The explosive is detonated from one end and the ensuing, planar reaction front is allowed to propagate in the axial direction down the length of the tube. Simple in concept, the experiment must be painstakingly conducted ensuring strict mechanical tolerances with detailed knowledge of the metallurgy of the copper. These requirements are essential to assure that the test yields high-quality, reproducible data. For more information on the cylinder test experimental setup and data acquisition, see [4]. Finally, the most common approach of calibrating the JWL EOS parameters to the experimental data is to perform high fidelity, multimaterial, hydrodynamic simulations that modify the model parameters until detonation-induced barrel deformation agreement is obtained between simulations and experiments [3,5,6].

The described method of JWL EOS model calibration establishes a foundation for defining explosive-specific parameters, and does well to characterize the general behavior of expanding detonation products. However, some comments can be made regarding the procedure. It is known that despite the significant care used to manufacture the explosive material (which is usually a blend of explosive chemical components along with some binder), the processed material may still contain imperfections. Realized by joints, cracks, holes, and gaps, explosive material blemishes can result in peculiar flow features whose origins are not fully understood [7]. These material defects lead to variations in experimental data that are unable to be properly represented by simulations that assume the explosive material to be perfectly homogeneous. Further, the copper in simulations of the cylinder tests requires a model to describe its dynamic behavior under the extreme conditions of detonation. As stated above, special attention is given to the metal used in the experiments to ensure it is of the highest purity. This effort serves to minimize the discrepancy between copper's physical behavior and its representation in the simulations. The cumulative effect of these inescapable shortcomings, in addition to experimental measurement uncertainties and setup nuances, is shot-to-shot variability. The data processing then involves an empirical fitting form to compile the experimental results [4]. Regardless, an EOS is able to be developed that captures the behavior of detonation products in the controlled experiments.

Various efforts have been performed that provide alternative methods for calibrating JWL parameters. One such practice, less prevalent in the literature, employs a thermo-chemical equilibrium code with built-in empirical relations to obtain the necessary energy release and volume information. A JWL parameter fitting algorithm then solves for optimum JWL parameters [5]. Analytic models have also been developed, e.g., the works of [3] and [5], that use idealized cylinder deformation dynamics along with energy relations to construct a set of equations that may be solved via an iterative scheme with experimental data. For both cases, optimized JWL parameters are obtained that show close agreement with the literature and numerical simulations.

In practice, the simulation of an explosive experiment involves the consideration of several modeling details in addition to the choice of detonation products EOS. For example, one must determine whether the chemistry model, unsteady and three-dimensional effects, shock-to-detonation process, interactions with the case, underlying reactant material microstructure, case modeling and expansion under extreme loads, etc., are important contributing factors to the physical results of interest [2,8,9]. Further, the uncertainties in the physics models, material defects in the solid explosive and casing, and uncertainties in the JWL parameters themselves often result in discrepancies between the results of simulations and experiments. Thus, it is common to make simplifying assumptions to reduce the complexity of the problem and draw focus to the driving physics of interest. In this work, the focus is to capture the macroscale flow of shocked air and detonation products induced by the detonation of a high explosive charge. Therefore, more emphasis is placed on the modeling of the detonation products and geometry as a whole, and less on the details of the complex detonation process and solid casing interaction. Here, the detonation is modeled using a reactive-burn formulation and propagates through homogeneous reactant material, confined within a rigid casing. In this configuration, the computational expense of a simulation is minimized while retaining the rich

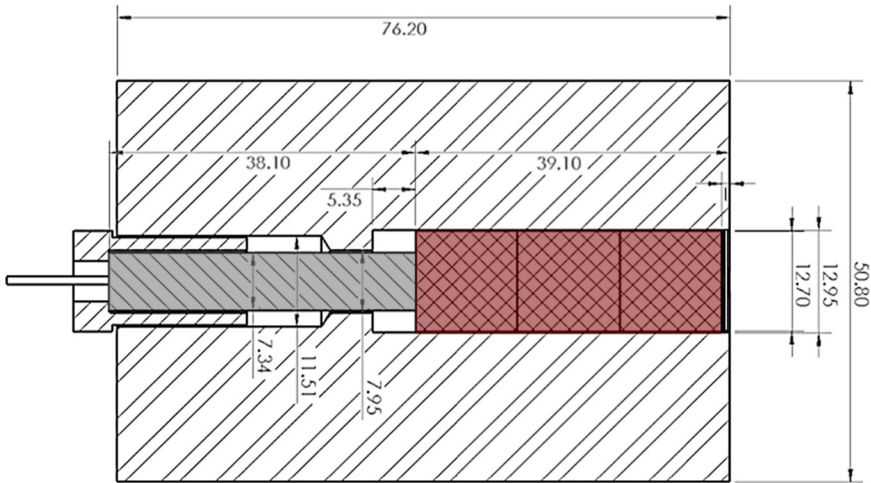


FIG. 1. A schematic showing a cross section of the explosive casing in the experiment. All dimensions are given in millimeters. The explosive train is described from left to right beginning with the RP-83 detonator, followed by three PBXN-5 pellets.

physics of the rapidly expanding flow. The current aim is to provide a method for reducing the error in the flow prediction of an explosive experiment. In many situations it is only possible to perform a given experiment a few times, so it is important that the simulation be able to predict the flow of a given realization with bounded uncertainty.

In this work, the explosive-specific model parameters of the JWL EOS are calibrated to an experimental geometry using uncertainty quantification techniques. High-speed photographs enable the primary shock position to be defined as a function of time and compared with simulations. With this information, JWL parameters are optimized to reduce the prediction error of the transverse shock position. The exact values of the optimized JWL parameters are specific to the present experimental configuration, which has been used in a series of experiments investigating detonation-driven explosive dispersal of large- and small-sized particles [10,11]. The calibrated post-detonation flow can then be used to evaluate particle motion and dispersion for comparison against the experiments. Furthermore, the method described in this work is applicable to any problem involving detonation-driven flow.

The paper will proceed as follows. Section II will detail the experiment to be simulated, Sec. III describes the simulation setup, Sec. IV will discuss the numerical methods and physical models used in the simulations, and Sec. V will explain the uncertainty quantification techniques and results, followed by the conclusions in Sec. VI.

II. EXPERIMENTAL SETUP

The explosive experiments simulated in this work were performed at the Munitions Directorate of the Air Force Research Laboratory at Eglin Air Force Base. The experiments are described thoroughly in [10] and a brief overview is given here. The experimental setup consists of a steel, cylindrical explosive casing with an inner diameter of 12.95 mm and outer diameter of 50.8 mm. Encased within the bore are three cylindrical explosive pellets of PBXN-5 (95% HMX/5% Viton A by weight) [12] laid end to end, each nominally 12.7 mm in diameter and length. The explosive pellets are detonated with a Teledyne RISI RP-83 detonator inserted from the rear of the assembly. Photographs of the experimental setup are available in [10] and a schematic of the explosive assembly is presented in Fig. 1. The detonation products expelled from the barrel immediately following the explosion were optically opaque and easily observed in the experimental images.

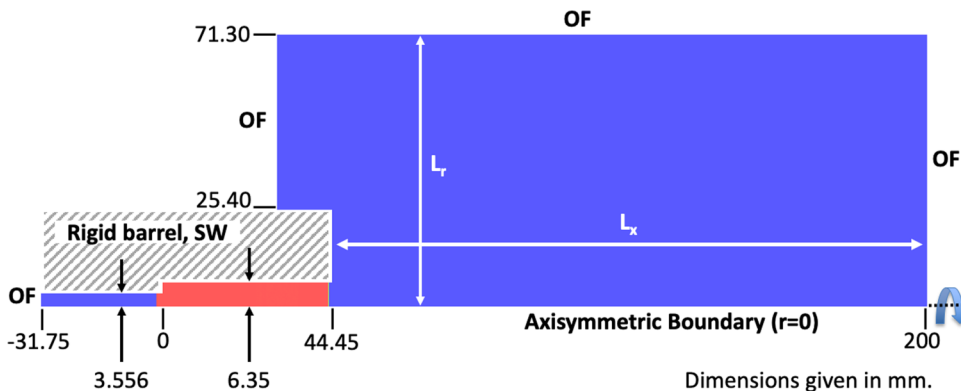


FIG. 2. Initial conditions for simulation of the experiment with dimensions and boundary conditions labeled; OF is an outflow and SW is a slipwall. All boundaries associated with the rigid barrel (labeled) are slipwalls. The blue colored regions are ambient air, while the red region shows the position of the explosive products immediately following the complete detonation of the PBXN-5 pellets.

High speed photographs of the explosive events used a Specialized Imaging SIMACON sampled at 666 kHz with a resolution of 1260×940 . Lighting for the images was provided by a Xenon flash lamp. The leading shockwave distorted light in the images, allowing its propagation to be observed.

Deformation of the explosive casing was observed following the explosive tests; see [10]. From the x-ray images provided in [10], an estimate of the casing deformation may be computed. It is estimated that the outer diameter of the explosive grew to 60.3 mm, whereas the pre-shot outer diameter of the casing was 50.8 mm, as shown in Fig. 1. This corresponds to an 18.7% increase in outer diameter. This deformation can augment the flow of explosive products being expelled from the casing, compared to a casing that were perfectly rigid. In this work, this solid deformation is not explicitly modeled in the simulations. Instead, the explosive-specific parameters of the equation of state of the explosive material are carefully adjusted, using uncertainty quantification techniques, to reduce the error in the flow prediction. The equation of state and uncertainty quantification procedure will be discussed in detail in Secs. IV and V, respectively.

III. SIMULATION SETUP

The symmetry of the experimental setup about the longitudinal axis of the barrel permits the simulations to be performed in an axisymmetric configuration. To achieve this computationally, the cylindrical form of the governing equations is solved where the centerline of the explosive assembly is simulated as a symmetric boundary on a two-dimensional, uniform, Cartesian grid with the axisymmetric assumptions applied. Boundaries of the simulation domain imposed by the solid walls of the explosive assembly are modeled as slipwalls. The simulated length in front of the barrel (L_x) is defined by the maximum distance present in the experimental data and is terminated by an outflow (OF) boundary condition; see Fig. 2. The radial extent of the domain normal to the centerline (L_r) is chosen to be tall enough to observe the transverse expansion of the explosive products and shock trajectory for comparisons with experimental data. This boundary is also treated as an outflow. The thin channel that holds the RP-83 detonator in the rear of explosive assembly allows explosive products to exhaust through the back of the assembly through an outflow. The details of the detonator are not simulated. The explosive region is initialized to replicate the design of the experimental setup. The high-explosive (HE) material is positioned such that the trailing edge of the final pellet to detonate is submerged by 1 mm within the barrel; see Fig. 1. Along the inner wall of the barrel, which forms the outer boundary of the initial detonation products, a slipwall (SW) boundary condition is applied.

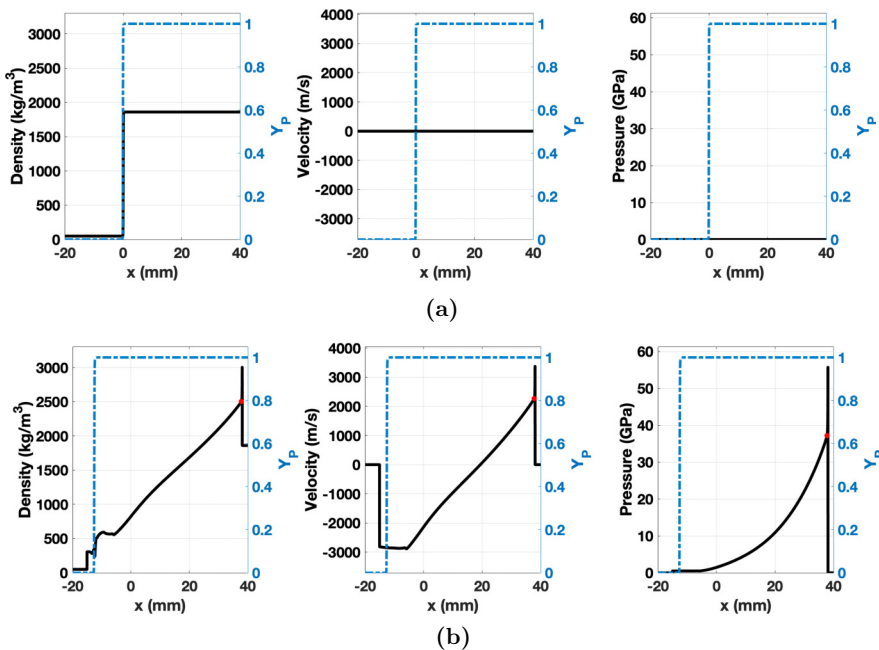


FIG. 3. Detonation simulation initial conditions and post-detonation flow profiles are shown in (a) and (b), respectively. The simulation completes when the detonation wave has reached the experimental length of the explosive pellets. (a) Detonation simulation initial conditions. The material interface (air-PBXN-5) is located at $x = 0$. Both materials start at rest ($u = 0$) at ambient pressure; (b) density, velocity, and pressure profiles upon complete detonation are shown. The simulation results shown here used the input JWL parameters of Table I. The detonation starts from the interface, initially at $x = 0$, and propagates to the right. The explosive products expand into the air, initially located at ($x < 0$). The mass fraction of explosive products Y_P is given on the right side axes. The location of the CJ state is shown by the red dot on each profile, where $\rho_{CJ} = 2512 \text{ kg/m}^3$, $u_{CJ} = 2295 \text{ m/s}$, and $p_{CJ} = 37.5 \text{ GPa}$.

The simulation of the experiment is performed in a two-step procedure: (i) First, the detonation of the explosive charge is simulated, (ii) the resulting density, velocity, and pressure profiles of the detonation simulation [see Fig. 3(b)] are extracted and read into the second simulation which solves the post-detonation expansion of the products into a larger domain. A separate code, described in Sec. IV B 2, is used in the first step to simulate the detonation of the PBXN-5 pellets. The detonation simulation solution profiles are only functions of x and are independent of the radial location. These results then form the initial condition for the state of the detonation products for the post-detonation simulation.

IV. NUMERICAL METHODS AND MODELING

For this work, the fluid is treated as a continuum field involving a mixture of two separate chemical species—the detonation products of the PBXN-5 charge and the surrounding, ambient air.

A. Fluid governing equations

The detonation-driven flow examined in this work is dominated by extremely high Reynolds number conditions, where viscosity will play only a minor role. Further, the time scales of interest are much smaller than the time required for considerable heat transfer by conduction. Finally,

resolving the boundary layer is computationally prohibitively expensive, and is out of the scope of this work. Neglecting the effects of both viscosity and conductivity, the governing equations for the fluid phase are the compressible, single-phase, and multispecies Euler equations. These equations are solved with a finite volume approach. The convective fluxes are computed using a second-order accurate AUSM+up scheme [13]. The calculated gradients are modified by using a WENO reconstruction method [14]. The time integration is performed with a third-order accurate Runge-Kutta scheme. The code which implements this entire solver has been previously tested and validated for a number of numerical simulations of compressible flows which involve shock waves [15–17].

Specifically, the following are the continuity, momentum, energy, and species evolution equations which are solved in this work in the Eulerian frame:

$$\frac{\partial \rho}{\partial t} + \nabla \cdot (\rho \mathbf{u}) = 0, \quad (1)$$

$$\frac{\partial(\rho \mathbf{u})}{\partial t} + \nabla \cdot (\rho \mathbf{u} \mathbf{u}) + \nabla P = 0, \quad (2)$$

$$\frac{\partial(\rho E)}{\partial t} + \nabla \cdot (\rho E \mathbf{u}) + \nabla \cdot (P \mathbf{u}) = 0, \quad (3)$$

and

$$\frac{\partial(\rho Y_P)}{\partial t} + \nabla \cdot (\rho Y_P \mathbf{u}) = 0. \quad (4)$$

In the above, the variables ρ , \mathbf{u} , and P are the gas density, velocity vector, and pressure, respectively. The specific total energy of the gas is represented by E and defined as

$$E = e + \frac{1}{2} \mathbf{u} \cdot \mathbf{u}, \quad (5)$$

where e is the specific internal energy of the fluid. In the species evolution equation, Eq. (4), Y_P is the mass fraction of the detonation products. If the mass fraction for the ambient air is desired, it is extracted from the constraint that $Y_{\text{air}} + Y_P = 1$. These equations are closed through a mixed-species equation of state for the thermodynamic variables (pressure, temperature, and speed of sound). This model will be explained in further detail in Sec. IV B 1.

B. Physical models

The fluid equation of state and detonation model are presented below, followed by the outflow boundary conditions for this problem.

1. Equation of state

The ambient air will be described using the ideal (or perfect) gas equation of state. The pressure and temperature of the ambient air as a function of density and specific internal energy are

$$P(\rho, e) = \rho e(\gamma - 1) \quad \text{and} \quad T(\rho, e) = \frac{P(\rho, e)}{\rho R} = \frac{e}{C_v}. \quad (6)$$

In the above, C_v is the specific heat of the fluid at constant volume, R is the specific gas constant for the fluid, and $\gamma = C_p/C_v$ is the ratio of specific heats for the fluid. In this work, $\gamma = 1.4$ and $R = 287 \text{ J/kg K}$.

Immediately after detonation, the temperatures and pressures of the products of detonation are on the order of several thousand degrees Kelvin and tens of thousands of atmospheres. These are well outside of the ranges where the ideal gas equation of state is a reasonable approximation. A real gas equation of state must be used to describe the detonation products. In this work, the

TABLE I. JWL parameters for LX-10-0 [21] and corresponding CJ state.

A (GPa)	B (GPa)	ω	R_1	R_2	ρ_0 (kg/m ³)	Q (MJ/kg)	D_{CJ} (km/s)	P_{CJ} (GPa)
880.200	17.437	0.30	4.60	1.20	1860	5.59	8.821	37.5

Jones-Wilkins-Lee (JWL) equation of state [18–20] is used for the products. These give the pressure and temperature as

$$P(\rho, e) = A \left[1 - \frac{\omega}{R_1 V} \right] \exp(-R_1 V) + B \left[1 - \frac{\omega}{R_2 V} \right] \exp(-R_2 V) + \omega \rho e, \quad (7a)$$

$$T(\rho, e) = \frac{1}{C_v} \left[e - \frac{A}{R_1 \rho_0} \exp(-R_1 V) - \frac{B}{R_2 \rho_0} \exp(-R_2 V) \right], \quad (7b)$$

under the assumption of a constant specific heat at constant volume. In the above, A , B , R_1 , R_2 , and ω are material-specific constants that researchers have determined through curve fits of data obtained from detonation experiments. Also, $V = \rho_0/\rho$ with ρ_0 being the initial, unreacted density of the explosive material. Table I gives the JWL model parameters and corresponding Chapman-Jouget (CJ) state values for these constants for LX-10-0, a high-explosive material compositionally identical to PBXN-5 (95% HMX, 5% Viton-A by weight) [12,21]. The parameters for LX-10-0 were used for numerical simulations since they are more readily available in the literature. Aside from Table I, the remainder of this paper will refer to the high-explosive material as PBXN-5.

As the high-energy detonation products are propelled outward into the ambient air, the two species of fluids will mix. The mixture requires a different equation of state to properly describe the local pressure and temperature. To reduce the computational complexity and cost, the equation of state for the mixture is obtained by modifying Eqs. (7a) and (7b). Specifically, the JWL constants of A and B are modified into a linear function of the mixture specific internal energy, while ω and C_v for the fluid are modified into linear functions of mixture density. These adapted parameters are implemented only where the mass fraction of explosive products is less than 99%; otherwise the JWL parameters for pure products are used.

The value used for ρ_0 in this work was obtained from experimental measurements of the explosive pellet density [10], and is different from what is given in [21]. The mean value and uncertainty associated with the measurements of ρ_0 are discussed in Sec. VC. The JWL equations for PBXN-5 given by (7a) and (7b) along with the values listed in Tables I and II will decay to become the ideal gas equations given by (6) in the limit when $\rho \rightarrow \rho_a$ and $e \rightarrow e_a$. However, it will allow for real gas behavior at moderate to high values of density and energy, $\rho \rightarrow \rho_0$ and $e \rightarrow e_0$. It should be noted that at the values of ρ and e given for pure PBXN-5 in [12,21], this modified equation of state also reverts back to the pure JWL equations. Thus, the blended equation preserves the correct asymptotic behaviors.

TABLE II. Model constants for PBXN-5 and air mixtures.

Model constant	Value	Units
ρ_a	1.258	kg/m ³
ρ_0	1796	kg/m ³
e_a	0.2	MJ/kg
e_0	5.6	MJ/kg
$C_{v,a}$	717	J/kg K
$C_{v,0}$	516	J/kg K

The mixture JWL equation of state proposed here is of empirical form, blending the JWL and ideal gas forms in a linear manner. The predictive capability of this model has not been rigorously defined, so an estimate of its error is provided here. Using simulation flow field results, approximately 300 data points of (ρ, p, e, Y_P) were extracted and used for error analysis. The sampling points were collected from the detonation products-air mixture region of the flow, where $0 < Y_P < 1$, and along the centerline. Samples were taken over all time that the material interface existed within the computational domain. The common approach for computing the multispecies mixture pressure is to constrain the system based on component pressure and temperature equilibrium. This nonlinear system may be solved iteratively, the details of which are given in [22] and are not repeated here. The density, internal energy, and mass fraction of the sample points collected from the simulation were used as inputs to the iterative mixture EOS solver of [22] to compute the p-T equilibrium mixture pressure. For mass fractions less than 0.5, the relative error in pressure remains below 10%. The error presented here is intended to give an order of magnitude estimate of the performance of the proposed EOS. The errors are computed while considering the p-T equilibrium result to be the true value. However, this result is inherently based on the thermal models of the JWL and ideal gas EOSs, which are limited in their own accuracy and range of applicability [23]. Further, the constraint that the temperature has equilibrated between the air and detonation products during the times of interest may not be entirely physical. Based on these considerations, the error computed between the two mixture EOSs is acceptable. It is recognized that the mixture EOS model may play a role in the detonation products EOS parametrization of Sec. VC. The influences of the model constants of the proposed mixture EOS are not explicitly considered in the model parametrization, but are expected to have a small effect on the parametrization of the variables on which they operate, namely A, B, and ω .

2. Detonation model

The rigid, steel barrel in the experiment acts as a channel for the explosive products, directing the gaseous mixture to expand axially after it is ignited from the leftmost end (refer to Fig. 1). The main charge of PBXN-5 has a length-to-diameter ratio $L/D \sim 3$, and most shock-to-detonation studies show that transition to detonation occurs before the length of the explosive [9]. It is assumed that the detonation products of the main PBXN-5 charge will dominate the flow following the detonation, so the details of the detonator are neglected. In the experiment, the products flow may be influenced by detonation front curvature and unsteady effects. In the simulations, it is assumed that flow gradients of the dense gas normal to the centerline during the detonation will be small relative to the gradients in the stream-wise direction. Thus, a reasonable description for the explosive products following the complete detonation can be obtained from a one-dimensional detonation simulation. The detonation code used in this work solves the reactive Euler equations and implements a density-based burn model along with the JWL equation of state to simulate the detonation of the PBXN-5 pellets in one dimension. The two material, one-dimensional reactive Euler equations are given by

$$\frac{\partial(\rho_1\phi)}{\partial t} + \frac{\partial(\rho_1\phi u)}{\partial x} = 0, \quad (8)$$

$$\frac{\partial(\rho_2(1-\phi))}{\partial t} + \frac{\partial(\rho_2(1-\phi)u)}{\partial x} = 0, \quad (9)$$

$$\frac{\partial(\rho u)}{\partial t} + \frac{\partial(\rho u u)}{\partial x} + \frac{\partial P}{\partial x} = 0, \quad (10)$$

$$\frac{\partial(\rho E)}{\partial t} + \frac{\partial((\rho E + P)u)}{\partial x} = Q\Omega, \quad (11)$$

$$\frac{\partial(\rho Y_R)}{\partial t} + \frac{\partial(\rho u Y_R)}{\partial x} = -\Omega, \quad (12)$$

and

$$\frac{\partial \phi}{\partial t} + u \frac{\partial \phi}{\partial x} = 0. \quad (13)$$

In the above equations the symbol ϕ represents the volume fraction of material 1, and $(1 - \phi)$ is the volume fraction of material 2. The subscripts 1 and 2 for $\rho_{(\cdot)}$ indicate the density of material 1 or 2, respectively. The density of the mixture is obtained by

$$\rho = \rho_1 \phi + \rho_2 (1 - \phi). \quad (14)$$

A continuum description of the air-PBXN-5 material interface would have a discontinuity at the transition point between the two different materials, where ϕ would instantaneously rise from 0 to 1 as one moves between materials. In the numerical simulation, a small number of grid points over a thin region are used to smoothly transition one material to the other. As in Sec. IV A, the variables P , u , and E are the pressure, velocity, and specific total energy, respectively. The specific total energy is defined as

$$E = e + \frac{1}{2} u^2, \quad (15)$$

where e is the specific internal energy. In Eq. (12), Y_R is the mass fraction of the reactant, in this case PBXN-5. The right-hand side of the energy equation contains the power deposition term, where \mathcal{Q} is the energy release per unit mass of the reactant and Ω is the reaction rate. The reaction is modeled as a single-phase with one-step chemistry using the same JWL EOS for both reactants and products. To obtain the initial physical state of the unreacted explosive, the EOS is modified by the factor $Y_R \Delta e$. The energy offset Δe is computed given $(\rho_0, P_0, e_{0,r})$. Mathematically, Δe is given by

$$\Delta e = -e_{0,r} + \frac{1}{w \rho_0} \left(P_0 - A \left[1 - \frac{\omega}{R_1} \right] \exp(-R_1) - B \left[1 - \frac{\omega}{R_2} \right] \exp(-R_2) \right), \quad (16)$$

where the ratio $V = \rho_0/\rho$ has been taken as unity, $e_{0,r} = 0$ and $P_0 = 102\,300$ Pa. This factor is only important during the detonation in the region where $Y_R > 0$, elsewhere this term has no effect. So the JWL EOS during the detonation is given by

$$P(\rho, e) = A \left[1 - \frac{\omega}{R_1 V} \right] \exp(-R_1 V) + B \left[1 - \frac{\omega}{R_2 V} \right] \exp(-R_2 V) + \omega \rho [e + Y_R \Delta e], \quad (17)$$

where the energy release due to chemical reaction appears as a source term in the energy equation. The adapted JWL parameters are used at the mixture region of air and explosive products, as described in Sec. IV B 1.

The current work employs a density-based burn model, with Ω defined as

$$\Omega = \rho [R_I + R_G], \quad (18)$$

where

$$R_I = k_I Y_R^{M_1} (1 - \rho/\rho_0)^{M_2} \quad (19)$$

$$\text{and } R_G = k_G Y_R^{N_1} (1 - Y_R)^{N_2} (\rho/\rho_0)^{N_3}. \quad (20)$$

Here, R_I and R_G are ignition and growth terms, respectively, ρ_0 is the initial unreacted density of the explosive, and $M_1, M_2, N_1, N_2,$ and N_3 are constants. As is typical in the ignition and growth literature, these terms are functions of the reactant mass fraction Y_R and mixture density ρ [9]. Previous work in calibrating explosives at the macroscale to experimental data yield $M_1 = N_1 = N_2 = 1$, $M_2 = 4$, and $N_3 = 2$ [24]. The values used for k_I and k_G are tuned to drive the reaction zone thickness of the detonation wave to experimental data. The reaction zone begins at the shock wave front that incites the chemical reaction and ends at the position where reactants have been depleted. It is in this region that large amounts of energy are released into the flow. The thickness of this region has profound effects on the detonation speed, minimum size of the explosive, and

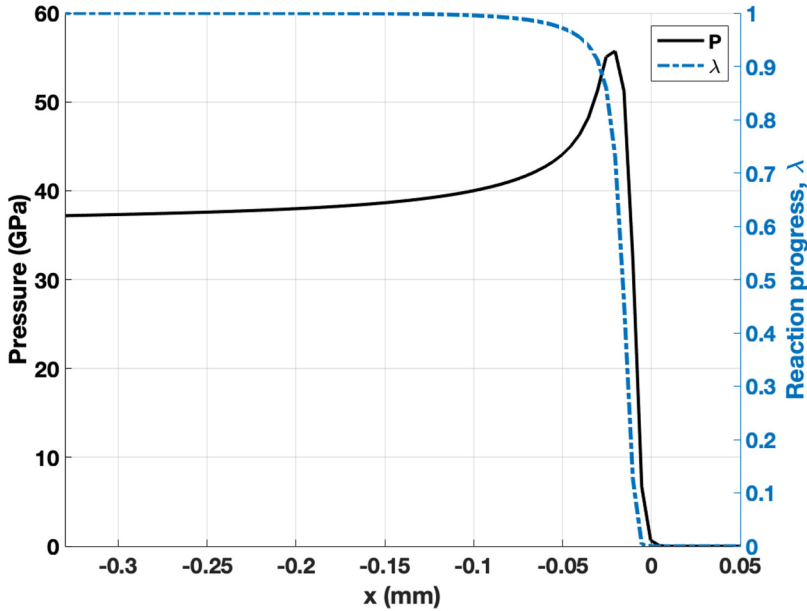


FIG. 4. The steady, 1D ZND reaction zone structure of Fig. 3(b) is plotted with respect to the shock front ($x = 0$, $\lambda = 1 - Y_R = 0$), and terminates where the reaction has ceased (CJ point, $\lambda = 1$, $Y_R = 0$). The reaction model is given by Eqs. (18)–(20). The predicted detonation velocity was 8.80 km/s.

input pressure required to support or initiate a detonation [25]. The current one-dimensional model assumes the explosive material to be homogeneous, and the reaction rate model will not affect the steady-state detonation speed or detonation pressure. In this formulation, the reaction rate model will only influence the formation of the detonation wave from the initial hot spot, and the flow variation through the reaction zone. Parameter sets resulting in physically reasonable reaction zone thicknesses have a small effect on the macroscale post-detonation flow, relative to the influence of the EOS parameters. Therefore, the uncertainties in the reaction rate parameters are not considered in this work. The exact values for k_I and k_G used in this work are $5.00 \times 10^9 \text{ s}^{-1}$ and $5.00 \times 10^7 \text{ s}^{-1}$, respectively, resulting in a reaction zone thickness of $\sim 0.2 \text{ mm}$. With the cell spacing at $5 \mu\text{m}$, approximately 40 grid points are used to resolve the reaction zone. Increasing the simulation resolution led to only minor changes in the sharpness of the leading edge of the reaction zone. Thus, grid convergence for simulating the detonation was established as $5 \mu\text{m}$, and agrees with the current literature [8].

The detonation simulations are performed using a finite-volume framework with the governing equations advanced in time using the third-order Runge-Kutta method. Flux computation uses the HLLC approximate Riemann solver. Further technical details on the detonation modeling methodology may be found in [24]. The simulation density, velocity, and pressure profiles at initialization and complete detonation are shown in Fig. 3. In Fig. 3(b) the detonation wave has propagated from the material interface, initially located at $x = 0$, into the high density, reactive material, initially at $x > 0$. The position of the expanding detonation products is shown by mass fraction on the right side axes. The steady detonation Zel'dovich-Neumann-Döring (ZND) structure is observed. This structure is composed of a “von Neumann spike” of compressed, unreacted material leading the detonation wave immediately followed by the reaction zone; see Fig. 4. The point in the flow where reaction has completed and flow gradients begin to decrease is the CJ point. It is within this reaction zone that energy is released to drive and sustain the detonation.

Following the simulations of the detonation, the resulting one-dimensional solution profiles of density, velocity, and pressure [see Fig. 3(b)] are interpolated onto the grid for the simulation of the

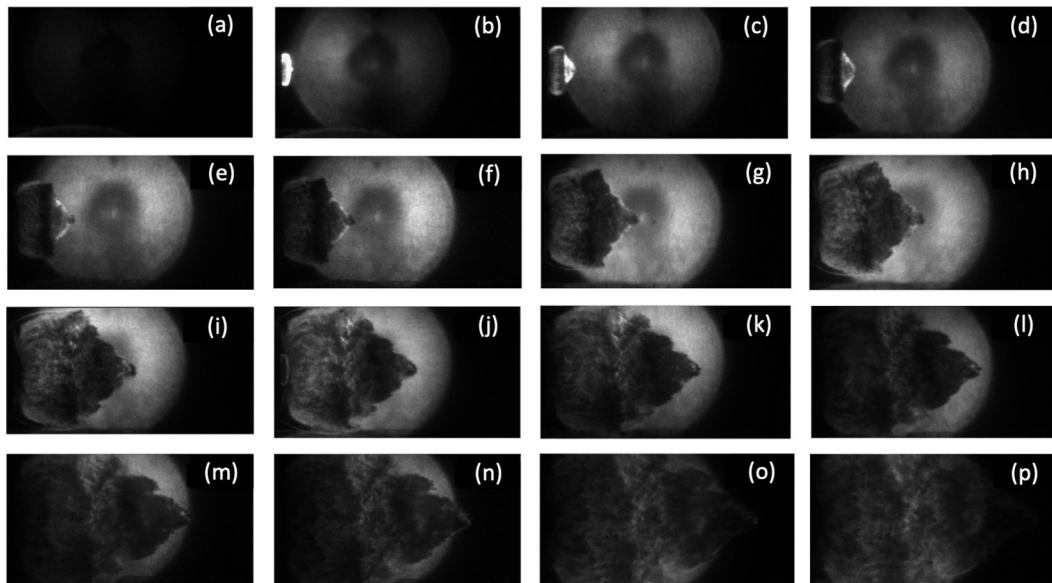


FIG. 5. High speed experimental images of the explosive event captured with the SIMACON camera (exposure time $0.3 \mu s$). The frames are in chronological order from (a) to (o) and equally spaced in time, with frame (a) at $t_{\text{exp}} = 12 \mu s$ with $\Delta t = 1.5 \mu s$. The visibility of the transverse shock is best in images (f)–(i), seen propagating toward the top and bottom of the frames. Optically opaque explosive products display a leading point near the center of the frames.

experiment (see Fig. 2). The initialization in the post-detonation simulations does not include the rearward traveling air shock from the detonation simulation. The explosive products are initialized in the second simulation such that they begin at the farthest location that the explosive products expanded away from the detonation wave and end at the leading edge of the reaction front.

3. Outflow boundary condition

As stated in Sec. III, the boundaries of the computational domain are chosen such that the maximum distances included in the experimental data are contained. This also defines the time over which the governing equations are integrated in the simulations. Over this duration, the outgoing blast wave and contact discontinuity reach the outer boundaries of the computational domain. As we do not want any nonphysical reflections of these outgoing waves, the characteristics-based approach for outflow boundary conditions developed by Thompson [26] and later by Poinot and Lele [27] is employed at all outflow boundaries. This allows flow discontinuities to pass through the outflow boundaries without spurious reflections.

V. RESULTS

In this section, the transverse shock propagation results of the simulations are compared with experimental data. Uncertainties in parameters of the equation of state and detonation model are shown to have strong influence on the prediction of the shock trajectory, and are calibrated to the experimental data using uncertainty quantification methods (Sec. VC). High speed photographs taken during the experiments (see Figs. 5 and 6) provide a detailed view of defining features of the explosive flow as it rapidly evolves; see Sec. II for imaging details. Careful analysis of these images enabled the transverse shock to be tracked and defined as a function of time.

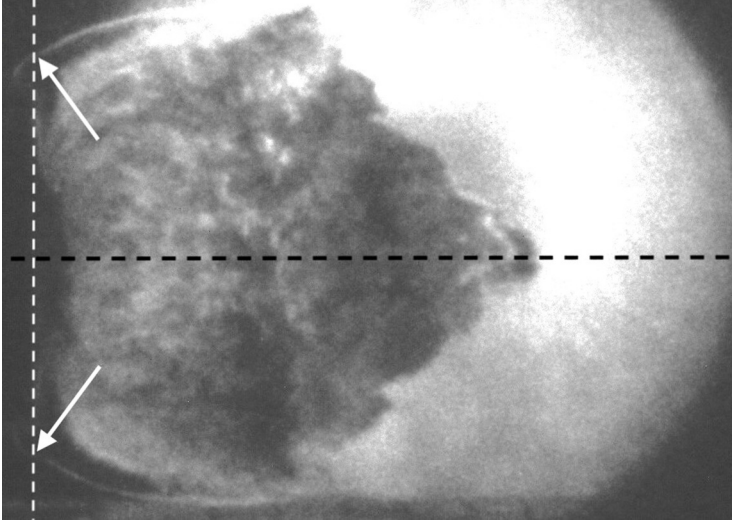


FIG. 6. Frame (i) of Fig. 5 is shown at a larger scale, with white arrows labeling the transverse shock. The white dashed line indicates the axis along which the transverse shock is tracked ($x = 44.45$ mm), and the black dashed line is the centerline of the explosive assembly. The image processing results of the transverse shock position are provided in Table III.

A. Grid resolution study

The extreme energy content and sharp gradients observed in the post-detonation explosive profiles necessitate a high degree of resolution to obtain a converged flow solution. We require highly resolved initial condition profiles of the post-detonation pressure, density, velocity, and thermal states of the detonation product to be well captured in the simulation for the resulting flow solution to be independent of the grid spacing. A grid-resolution study was performed to monitor the trajectory of the primary shock along the centerline as the grid spacing is varied in the simulation with the initial condition held constant. The test employs the post-detonation explosive profile with maximum energy for the initial condition at grid spacings of $200\ \mu\text{m}$, $100\ \mu\text{m}$, $50\ \mu\text{m}$, and $25\ \mu\text{m}$. The grid-independent initial condition is obtained by interpolating the highly resolved explosive profile to the lowest resolution grid, and the resulting interpolated profile is used as the initial condition for all grid sizes. The peak values of pressure, density, and velocity are positioned at the cell center whose face is located nearest to the experimental end location of the explosive to ensure consistent maximum values between grids. The steep gradients in flow properties leading to ambient conditions on either end of the explosive region are included in the interpolations of the initial condition to the finer grids. This is done in order to preserve the initial condition to be the same across all the grids simulated and prevent a sharpening of the driving flow gradients between the explosive region and the ambient conditions as the grid spacing is reduced. The results of the study are shown in Fig. 7. The position of the primary shock at a given instant is nearly the same between the simulations of $25\ \mu\text{m}$ and $50\ \mu\text{m}$, while the differences are significant for grids of larger grid spacing. From these results, the grid spacing at which solution convergence is observed is $50\ \mu\text{m}$.

B. Transverse shock

The transverse shock refers to the portion of the primary shock that immediately turns the corner of the barrel as it propagates outward. This metric was used due to its clear visibility in the experimental images, and is easily distinguished from the explosive products in this radial direction.

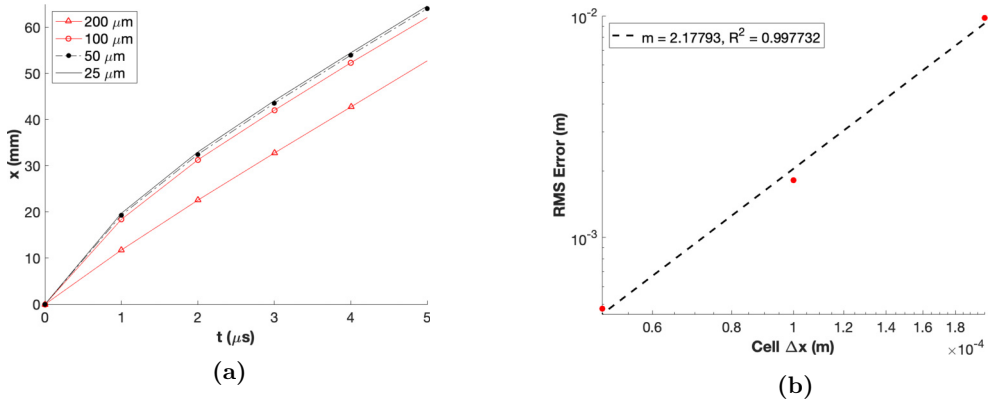


FIG. 7. Grid resolution study results. (a) Shown are the trajectories of the primary shock along the centerline, where the legend denotes the grid spacing used in each simulation. (b) Shown are the RMS errors (red circles) of shock position computed against the most resolved grid. The line of best fit is also provided. (a) Simulation shock trajectories along the centerline; (b) RMS errors with respect to the 25- μ m case.

The experimental transverse shock trajectory was extracted along a line tangent to the face of the barrel, and its position at each time was defined as the average of the shock locations above and below the centerline (images provided a side view of the explosive event). The uncertainty in timing for the shock position was given by the exposure time of the frames, 0.3 μ s. The uncertainty in the position of the shock was derived through a careful analysis of the barrel size during the explosive event, and was propagated through the processing of the images when extracting the shock position. The shock in the simulations was tracked along the same line tangent to the barrel face and its location was defined as the position where the pressure first rose to 10% above the ambient air pressure (see Fig. 8). It is noted that there is some uncertainty associated with the shock position in the simulations. The shockwave is represented by a smooth increase in flow variables that spans a few grid cells, rather than a perfect, step-function discontinuity. This uncertainty in simulation shock position is small relative to both the distance over which it is tracked, and the variation in its position due to JWL parameter uncertainties, and is not considered in this work.

Comparisons were made between simulations and experiments after time-shifting each simulation such that the position of the simulated transverse shock falls exactly on the first experimental data point. In this regard, the comparison between simulation and experiment may be understood as comparing the propagation speed of the transverse shock, imposing the assumption that the two originated from the same position and time. This was done to eliminate the uncertainties associated with detonator function time, shock-to-detonation transition, and reaction rate of the high explosive material. The experimental data points for the transverse shock position are given in Table III.

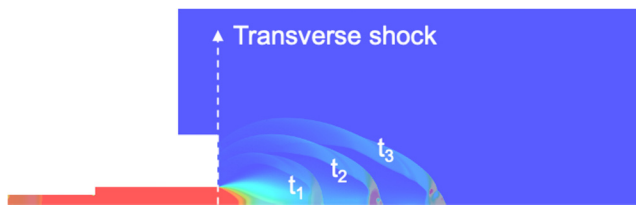


FIG. 8. Simulation pressure contour shown at three intermediate times. The position of the transverse shock is defined along the vertical dashed line at $x = 44.45$ mm.

TABLE III. Experimental data points of the transverse shock position over time. The data points are defined along the white dashed line shown in Fig. 6 at $x = 44.45$ mm. The uncertainty in position for each data point are given by e_r . The uncertainty in time for each data point e_t is ± 0.15 μ s.

t (μ s)	r (mm)	e_r (mm)
13.5	10.13	1.41
15.0	13.59	1.77
16.5	18.28	2.58
18.0	19.31	0.29
21.0	26.96	2.01
22.5	29.61	0.62
24.0	30.32	1.06
25.5	32.97	0.92
27.0	33.96	0.19
28.5	39.17	0.94
33.0	43.12	0.99
34.5	45.20	0.99

C. Explosive model calibration

The JWL parameters provided in Table I, namely A , B , ω , R_1 , and R_2 , are specific to the high explosive material composed of 95% HMX with 5% Viton-A by weight. These parameters are determined from curve fits to data obtained from cylinder test experiments that burn this specific explosive material. Accurately characterizing these energetic materials is not an easy task, and the data from these tests contain inherent uncertainties arising from measurement uncertainty, material defects, and other sources. Uncertainties in the data used to fit the JWL parameters results in uncertainties being introduced into the parameters themselves. Experimental density measurements of the explosive pellets gives the uncertainty in the initial density ρ_0 [10]. Lastly, modeling the reacting material involves a heat release quantity Q (see Sec. IV B 2), also determined from curve fits to dated and uncertain experimental data. In this work, the uncertainties of these uncertain parameters are considered and leveraged to reduce the error in the flow prediction. As this work is motivated by the interest to validate the particle force model for this flow regime, the simulation flow prediction must be in agreement with that seen in experiments. The uncertainty in each of the seven model parameters are carefully considered to permit a calibration of the parameters to experimental flow data, reducing the uncertainty in the prediction of the gas flow. For the model parameter calibration to experimental data, the transverse shock location is used as the metric due to its visibility in the experimental images, as stated in Sec. V B. Table IV summarizes the selected seven parameters and their uncertainties represented by range, along with the lower and upper bounds of the parameters. The range is defined as (max-min)/mean. In the calibration procedure, each one of the seven parameters is modeled as random variables that may take any value within the

TABLE IV. Uncertain model parameters with associated values and uncertainties.

Model	Detonation		JWL EOS				
	ρ_0 (kg/m ³)	Q (MJ/kg)	A (GPa)	B (GPa)	ω	R_1	R_2
Mean [21]	1796*	5.60	880.2	17.437	0.30	4.6	1.2
Range	0.94%*	30%	10%	10%	20%	20%	20%
Min.	1787	4.76	836.2	16.564	0.27	4.14	1.08
Max	1804	6.44	924.2	18.303	0.33	5.06	1.32

*Experimental measurement of [10].

given range. The parameter uncertainty ranges were estimated by examining the literature values of the parameters for similar, HMX-based explosives.

Due to the computational cost of the simulations, it is necessary to filter out less influential parameters for the calibration. Such a process is called variable screening, and global sensitivity analysis (GSA) is utilized in this paper for that purpose [28–30]. The basic idea is that if a variation of a parameter does not cause a significant variation in the shock location, the parameter is not important and can be considered fixed. GSA measures individual parameters contributions to the variation of the shock location. Based on the GSA results, a reduced parameter set was obtained and calibration was carried out for the dominant variables.

1. Global sensitivity analysis

For the GSA, each of the seven parameters presented in Table IV is modeled as uniformly distributed random variables. GSA ranks the random input variables by comparing their contributions to the variance of the output. It is used to determine the most influential variables when the variable space dimension is high. GSA decomposes a function as a linear combination of subfunctions of increasing dimensions as

$$g(\mathbf{x}) = h_0 + \sum_{i=1}^n h_i(x_i) + \sum_{i=1}^n \sum_{j=i+1}^n h_{ij}(x_i, x_j) + \dots + h_{12..n}(x_1, x_2, \dots, x_n), \quad (21)$$

where n is the dimension of input variables and h_0 is a constant. The subscripts denote the variables corresponding to the subfunction. For example, h_{12} is a function of x_1 and x_2 . The subfunctions are decomposed in such a way that the inner products of two subfunctions vanish. That is,

$$\int_{\Omega_x} f_x(\mathbf{x}) h_{i_1, \dots, i_s}(x_{i_1}, \dots, x_{i_s}) h_{j_1, \dots, j_s}(x_{j_1}, \dots, x_{j_s}) d\mathbf{x} = 0, \quad i_1, \dots, i_s \neq j_1, \dots, j_s, \quad (22)$$

where $f_x(\mathbf{x})$ is the joint probability density function (PDF) of input variables. In the case of the uniformly distributed PDF, the subfunctions become the Legendre polynomials.

The main advantage of the decomposition in Eq. (21) is that the variance of the original function $g(\mathbf{x})$ can be also decomposed as the sum of the variance of the subfunctions as

$$V[g(\mathbf{x})] = \sum_{i=1}^n V[h_i] + \sum_{i=1}^n \sum_{j=i+1}^n V[h_{ij}] + \dots + V[h_{12..n}]. \quad (23)$$

The variance of a subfunction in Eq. (23) is calculated by definition as

$$V[h(\mathbf{x})] = \int_{\Omega_x} [h(\mathbf{x}) - E(h(\mathbf{x}))]^2 f_x(\mathbf{x}) d\mathbf{x}, \quad (24)$$

where $E(\cdot)$ denotes the expected value of a function, and $h(\mathbf{x})$ represents the subfunction under consideration.

Equation (23) may be used to define a sensitivity index that shows the contribution of each variable to the output variance. This sensitivity index is given as

$$S_{i,j..r} = \frac{V[h_{i,j..r}]}{V[g(\mathbf{x})]}. \quad (25)$$

A sensitivity index corresponding to a single variable $V[h_i]$ is called the main sensitivity index. If the index corresponds to two or more variables, it is the interaction sensitivity index. In this paper, the main sensitivity index was used to determine the important variables.

To perform the GSA, 66 Latin hypercube samples (LHS) of $(A, B, \omega, R_1, R_2, \rho_0, Q)$ were obtained to construct a surrogate model based on the simulation output quantity of interest, the transverse shock trajectory. In general, it is recommended that the number of samples is about twice that of unknown coefficients in linear regression. For seven variables, if quadratic polynomials are

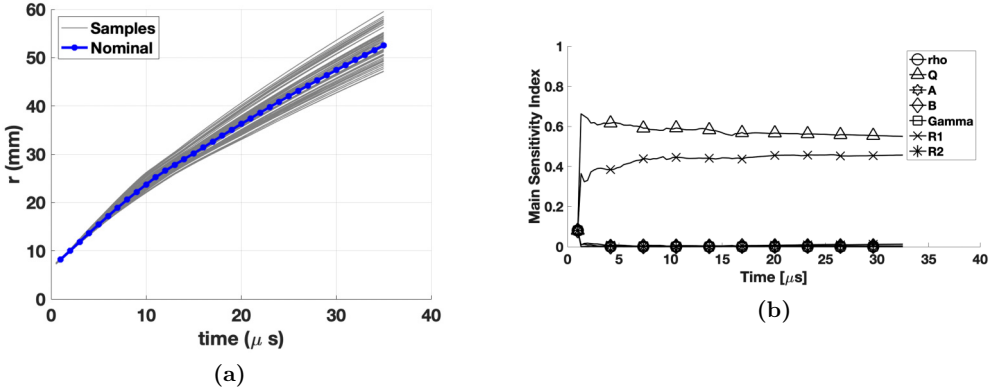


FIG. 9. Simulation transverse shock trajectories and corresponding GSA results. (a) Simulation transverse shock trajectories, 66 LHS samples over seven variables: A , B , ω , R_1 , R_2 , ρ_0 , Q ; (b) GSA results. The main sensitivity index of each uncertain variable is shown over time. The variables Q and R_1 are observed to be dominant in affecting the quantity of interest.

used, there are 36 unknown coefficients. Therefore, 66 samples is a reasonable number. However, the purpose of GSA is not estimating the quantity of interest (QOI) accurately but identifying significant variables. For that purpose, 66 LHS samples is acceptable. Figure 9(a) shows the trajectories of the 66 simulated transverse shocks corresponding to the sampled input parameters. GSA requires a substantial number of simulations for accurate calculation. Due to the limitation on computational resources, a surrogate model is used to predict the transverse shock location as a function of seven parameters based on a finite number of simulations. For this task, the chosen surrogate model was a Kriging model. A Gaussian process, Kriging assumes that the functional response follows a joint normal distribution correlated by a radial basis function [31,32]. The Kriging prediction comprises a trend function and a systematic departure as

$$f_{\text{KRG}}(\mathbf{x}) = \mathbf{b}(\mathbf{x})^T \boldsymbol{\beta} + Z(\mathbf{x}), \quad (26)$$

where in this work $\mathbf{b}(\mathbf{x})$ is a polynomial basis function vector, $\boldsymbol{\beta}$ is the coefficient vector, and $Z(\mathbf{x}) \sim N(0, \sigma^2(\mathbf{x}))$. Because the transverse shock location changes over time, a Kriging model is constructed for each time increment. Figure 9(b) shows the GSA results. The main sensitivity index reveals that the heat release Q and a model constant associated with pressure decay in the JWLEOS R_1 are the most important parameters affecting the simulation output QOI.

The response of the simulation shock propagation in the axial direction was also monitored. The position of the shock was defined along the centerline of the simulation domain, using the same data extraction method as for the transverse shock; see Sec. V B. The simulation axial shock trajectories for the 66 LHS samples, and corresponding GSA result, are presented in Fig. 10. In Fig. 10(a), the shock trajectories are plotted in the frame of the simulation domain, where the axial shock originates from the end of the detonated explosive at ($t = 0$, $x = 43.45$ mm). From the GSA, it is shown that the same parameters most strongly influencing the transverse shock propagation also dominate the shock propagation in the axial direction.

2. Parameter calibration

Based on the GSA results, another 37 samples of (Q , R_1) were generated. In these samples, all other five parameters (A , B , ω , R_2 , ρ_0) remained fixed at their mean values. For two variables, there are six unknown coefficients, so 37 samples is sufficient for calibration. In this case, more samples than necessary were used in order to increase the prediction accuracy. The sample locations are shown in Fig. 11(a) and corresponding transverse shock trajectories in Fig. 11(b), plotted with the

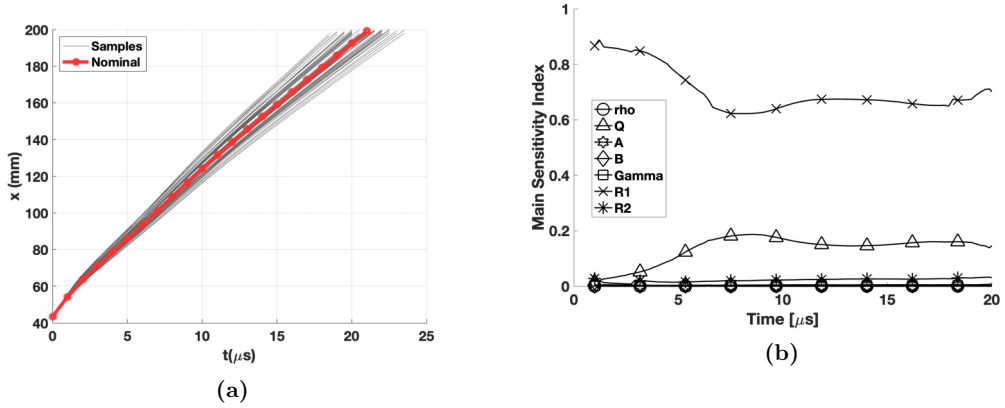


FIG. 10. Simulation shock trajectories along the centerline and corresponding GSA results. (a) Simulation shock trajectories along the centerline, 66 LHS samples over seven variables: A , B , ω , R_1 , R_2 , ρ_0 , Q ; (b) GSA results corresponding to simulation output shown in Fig. 10(a) (left). The main sensitivity index of each uncertain variable is shown over time. The variables Q and R_1 are observed to be dominant in affecting the simulation axial shock position; (a) simulation shock trajectories along the centerline, 66 LHS samples over seven variables: A , B , ω , R_1 , R_2 , ρ_0 , Q .

experimental data. It is noted that the simulation shock trajectories envelope the experimental data points, so that any extrapolation is avoided. Using the time-shifted simulation results (see Sec. VB) from these 37 runs, a polynomial response surface (PRS) was constructed for calibration. The PRS was chosen for this task as it requires fewer samples than Kriging to obtain an accurate prediction. The samples for the response surface are evenly spaced in time, every $3 \mu\text{s}$, from $13.5 \mu\text{s}$, the time of the first experimental data point, to $35 \mu\text{s}$, that of the last experimental data point. The basis function for the PRS is the following,

$$f_{\text{PRS}}(Q, R_1, t) = c_1 + c_2Q + c_3R_1 + c_4Q^2 + c_5QR_1 + c_6R_1^2 + c_7\log(t) + (c_8 + c_9Q + c_{10}R_1)t + e. \quad (27)$$

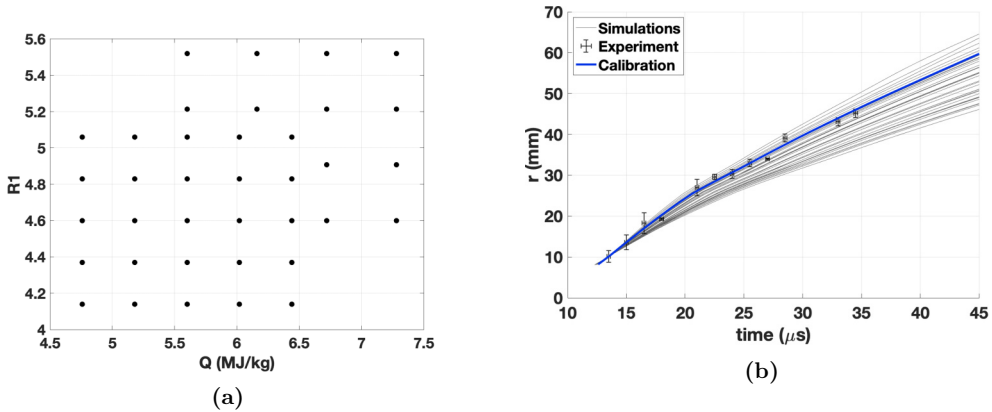


FIG. 11. Sample locations and simulation transverse shock trajectories for 37 samples of $Q - R_1$; (a) simulation transverse shock trajectories for the 37 samples of $Q - R_1$, along with the experimental data points of Table III.

TABLE V. Coefficients of PRS.

Coefficient	c_1	c_2	c_3	c_4	c_5	c_6	c_7	c_8	c_9	c_{10}
Value	1.53	-0.26	-0.35	0.04	0.07	0.09	0.82	0.06	0.05	-0.01

For Q and R_1 , quadratic basis functions are applied, whereas logarithmic and linear basis functions are used for t . The interaction terms Qt and R_1t are added to account for any overlapping behavior of the shock positions that might occur over time. The selection of the basis functions is heuristic. However, it represents the behavior of the shock position well. Before finding the coefficients in Eq. (27), the parameters, Q , R_1 , and t , were normalized to compare the relative effect of each polynomial basis function. For the normalization, the following equation is used:

$$x_N = \frac{x - x_L}{x_U - x_L} + 1. \quad (28)$$

Note that Eq. (28) normalizes a parameter remaining between 1 and 2 to avoid zero, because of the logarithmic basis function. The upper and lower bounds of each variable being normalized, denoted by x_U and x_L , respectively, are given in Table IV. The coefficients for the PRS are found by minimizing the root-mean-square error between the PRS and the simulation transverse shock data. Table V shows the coefficients found using the PRS with the normalized parameters. To validate the PRS model R^2 noise and prediction residual error sum of squares (PRESS) are provided: R^2 of the PRS is 0.9815, the noise is 0.00175, and the PRESS is 1.62 mm. For the parameter calibration, the root-mean-squared error (RMSE) is used, given by

$$e_{\text{RMS}}(Q, R_1) = \sqrt{\frac{1}{n_{\text{exp},t}} \sum_{i=1}^{n_{\text{exp},t}} (y_{i,\text{exp}} - y_{\text{PRS}}(Q, R_1; t_i))^2}. \quad (29)$$

Here, $y_{i,\text{exp}}$ is the experimental data point of the transverse shock location at time t_i , where $i = 1, 2, 3, \dots, n_{\text{exp},t}$. Also, $y_{\text{PRS}}(Q, R_1; t_i)$ is the PRS transverse shock location prediction at the same time t_i for a given (Q, R_1) . The optimum set of parameters is the one that minimizes the RMSE of Eq. (29). Figure 12 displays the contour of the RMS error in the domain of Q and R_1 , using the PRS with the mean experimental data. The optimum point in Eq. (29) was found at $(Q, R_1) = (6.32, 5.42)$. The simulation transverse shock trajectory using (Q, R_1) for this optimum point is compared with

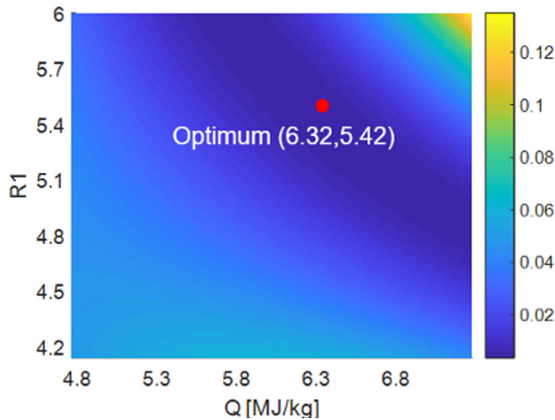


FIG. 12. Root-mean-square error contour using 37 samples in $Q - R_1$ space. Errors were computed with respect to the mean experimental data.

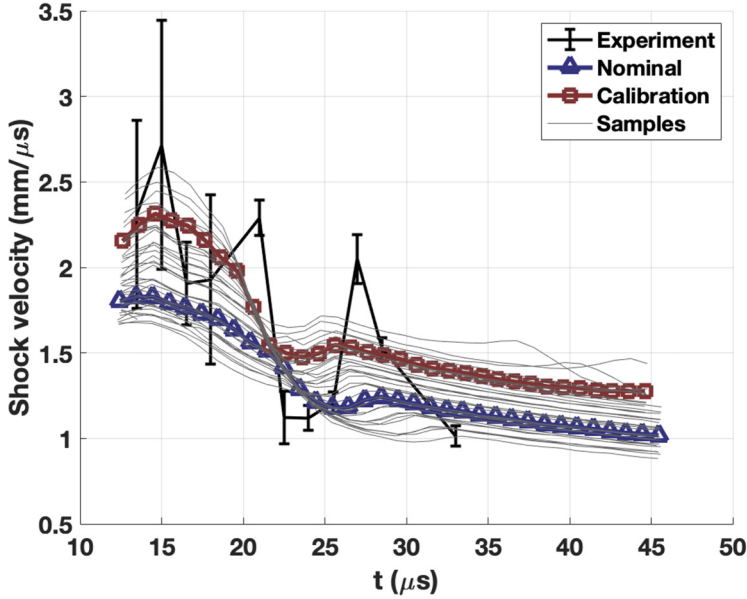


FIG. 13. The transverse shock velocity, associated with the data in Fig. 11(b), is shown. The uncertainty in the experimental transverse shock velocity was obtained by propagating the uncertainties in the shock position and time. Additionally, the transverse shock for the nominal set of uncertain model parameters is shown.

the experimental data in Fig. 11(b), labeled “Calibration.” The velocity of the transverse shock, associated with the simulation and experimental shock position data in Fig. 11(b) is shown in Fig. 13. The velocity at time t_k is estimated as the second-order, central difference approximation of the first derivative of position with time. The experimental shock velocity is assigned error bars at each time, which are the result of the propagation of the position and time uncertainties of the shock position data. The derived, experimental shock velocity contains considerable fluctuations and uncertainty, so a calibration based on this quantity was not performed.

3. Physical interpretation

The discrepancy between the optimum point, $(Q, R_1) = (6.32, 5.42)$, and the values of the literature (see Table IV) may be attributed to a combination of multiple factors. A readily apparent cause for some discrepancy is shot-to-shot variability, explained in Sec. I, but this may not account for the total difference. The forensic uncertainty quantification, detailed in [10], revealed that there was deformation of the steel explosive confiner in the experiments. This solid deformation, driven by the high pressure of detonation, acts to remove energy from the flow. As the steel barrel expands, the volume of the contained fluid increases and the pressure decays. The R_1 parameter in the JWL EOS controls the rate of pressure decay with volume. Therefore, the increased, calibrated value for R_1 is likely compensating for the influence of the barrel deformation on the resulting flow, where simulations model the barrel as a rigid boundary. In this sense, the calibrated R_1 value serves to increase the pressure decay rate as the fluid expands outside of the barrel, where the fluid pressure has begun to decay earlier in the experiment due to barrel deformation. The accompanying increase in Q serves to maintain the detonation pressure prior to the fluid expansion, as increases in R_1 lead to considerable pressure decrements for fixed values of (ρ, e) .

In the JWL EOS model [Eq. (7a)], the R_1 term determines the hydrodynamic response in regions where the fluid volume v is on the order of the unreacted volume v_0 . Here, in flow regions near the transverse shock, the fluid volume is much greater than that of the unreacted

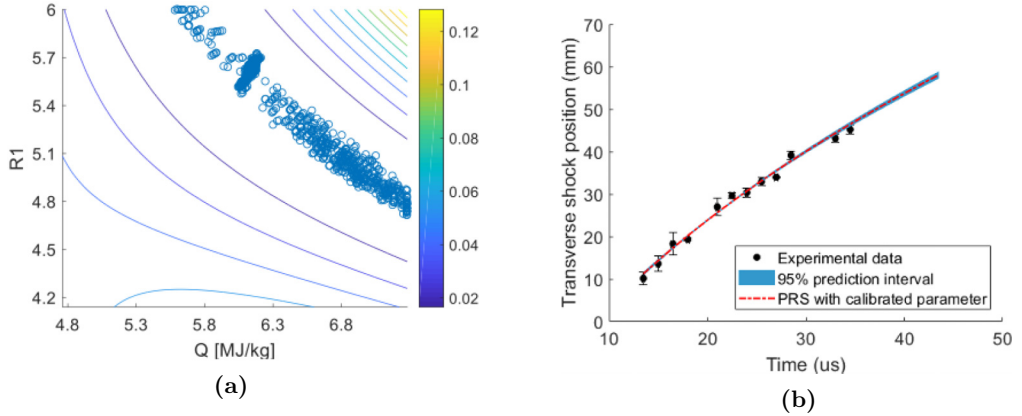


FIG. 14. Calibration process considering the measurement uncertainty. (a) Calibrated parameters for different sets of measurement samples; (b) PRS prediction with 95% confidence interval.

material, $\rho_0/\rho = v/v_0 \sim O(10^3)$. At the conditions near the transverse shock, the EOS model of Sec. IV B 1 will predict a behavior tending toward that of an ideal gas, and the R_1 term will not be particularly active locally. However, the shock is driven by an extreme flow of detonation products emanating from within the barrel. Inside the barrel, the fluid volume is such that the R_1 term will still significantly influence the pressure decay, and resulting fluid acceleration, of the driving detonation product “reservoir.”

4. Influence of measurement uncertainty

The measurement uncertainty affects the calibration process as well. Assuming the measurement uncertainties follow a uniform distribution, 1000 Monte Carlo simulation (MCS) samples of measurement data are generated to repeat the calibration process. Figure 14(a) shows the calibrated parameters using the MCS samples. Notice that the calibrated parameters form a curve in the domain, rather than a point. This means that the combination of the two parameters along the curve can result in similar shock propagation. This is the traditional example of nonunique identification of system parameters. It is interesting to note the strong relationship between the heat release parameter Q , and the JWL model parameter R_1 , with regard to shock propagation. The physical interpretation of such a relationship remains a topic of future research. Lastly, the transverse shock predictions using PRS model is plotted in Fig. 14(b). The blue shaded area represents the 95% confidence interval of the PRS prediction due to the measurement uncertainty. Considering the measurement uncertainty in the calibration of parameters resulted in only small variations in the transverse shock prediction. Figure 15 displays the calibrated simulation, corresponding to the mean prediction of PRS in Fig. 14(b), along with the simulation before calibration. For the purposes of this work, the calibration using the mean experimental data is sufficient (see Fig. 12).

VI. CONCLUSION AND FUTURE WORK

This work investigates the prediction of a detonation-driven flow using the Jones-Wilkins-Lee (JWL) equation of state (EOS) to model the detonation products. Explosive experiments pose a challenge to computational researchers due to the range of associated physical modeling considerations, detailed in the Introduction. In response, scientific studies of detonation events often use simple models, where appropriate, to manage the complexity of the problem and steer the focus toward the physics of interest. Here, we examine the extreme flow that is the result of an explosive test consisting of three cylindrical, high-explosive pellets being detonated from within an open-ended steel bore. As the current aim is to reduce the simulation prediction error in the transverse shock

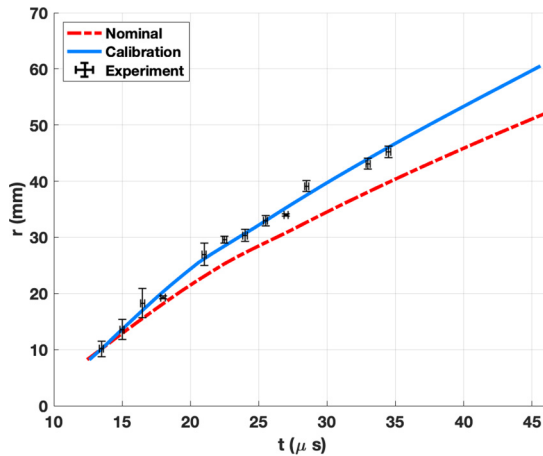


FIG. 15. Simulation transverse shock trajectories before and after calibration are shown, along with experimental data.

position, less emphasis is placed on modeling the complex detonation processes and more attention is given to the modeling of the detonation products and experimental geometry at the macroscale. Accordingly, a reactive-burn formulation is employed to simulate the detonation of homogeneous high-explosive material confined by a rigid outer casing. It is shown that the JWL parameters may be meticulously adjusted to reduce the prediction error in the shock position. Global sensitivity analysis (GSA) is employed to reveal the JWL parameters to which the transverse shock propagation is most sensitive. With GSA yielding two dominant parameters, a polynomial response surface is constructed that allows the optimum set of parameters to be determined. The prediction of the transverse shock following the parameter calibration agrees well with experimental data, where the RMSE is found to be 0.97 mm.

This investigation serves as a prerequisite study for a particle force model analysis in the detonation regime. Point-particle force models rely on flow properties at the particle location to predict the force on the particle due to the continuous phase fluid flow. Significant effort has been performed by past investigators examining the simplifying case of a single particle subjected to a modest shock, where the Maxey-Riley-Gatignol (MRG) force model extended for compressible flows, has been shown to perform well [33,34]. Now it is of interest to consider the force on a particle during the interaction with a stronger shock followed by a dense, explosive products contact interface, which is the result of the detonation of a high explosive material. Large-scale simulations of the explosive dispersal of particles often rely on point-particle models to manage the computational size of the problem, though the validity of the particle drag model in this regime has not been well studied. The accurate prediction of the shock propagation presented in this work provides confidence in the prediction of the post-shock gas flow, where typical flow measurements are unavailable. Particle trajectory data obtained from the same experiment may then be used to examine the predictive capability and sensitivity of the particle force model components in these extreme conditions.

ACKNOWLEDGMENTS

This work was supported in part by the US Department of Energy, National Nuclear Security Administration, Advanced Simulation and Computing Program, as a Cooperative Agreement under the Predictive Science Academic Alliance Program, under Contract No. DE-NA0002378.

APPENDIX: LEAST-SQUARES METHOD

The least-squares method is used in this work for the construction of the polynomial response surface (PRS) based on simulation results, and again for the parameter calibration which minimizes the error between the experimental data and the PRS. A simple description of the method is given below.

Let y_k denote a measurement of some data at time index k , and let z_k be a corresponding simulation output at the same time t_k . The measured data and simulation output may be related by

$$y_k = z_k + \epsilon_k, \tag{A1}$$

where ϵ_k is the error between the measurement and simulation. In general, the error can represent measurement error and error in simulation output. For simplicity, let us assume that the error is only due to measurement error and is randomly distributed with the mean error equal to zero, and that the simulation output contains no error. Let the simulation model $z(t; \theta)$ be a linear function of the input variable t as

$$z(t; \theta) = \theta_1 + \theta_2 t, \tag{A2}$$

$$\text{where } \theta = \{\theta_1 \theta_2\}^T. \tag{A3}$$

Here, θ is a vector of unknown parameters to be fit to the measurement data. The notation $z(t; \theta)$ is used to state that simulation takes the input variable t and depends on the parameter vector θ .

Let there be n_y data points of measurement data, such that the data may be represented by (y_k, t_k) , where $k = 1, 2, 3, \dots, n_y$. In vector form, the measurement data may be written as $\mathbf{y} = (y_1, y_2, y_3, \dots, y_{n_y})^T$. In the same way, the simulation model for n_y data points can be written as

$$\mathbf{z} = \begin{bmatrix} z_1 \\ z_2 \\ \vdots \\ z_{n_y} \end{bmatrix} = \begin{bmatrix} 1 & t_1 \\ 1 & t_2 \\ \vdots & \vdots \\ 1 & t_{n_y} \end{bmatrix} \begin{Bmatrix} \theta_1 \\ \theta_2 \end{Bmatrix} = \mathbf{X}\theta, \tag{A4}$$

where \mathbf{X} is known as the design matrix.

The vectors of measured data and simulation output may be used to define a vector of errors as $\mathbf{e} = \{\epsilon_1, \epsilon_2, \dots, \epsilon_{n_y}\}^T = \mathbf{y} - \mathbf{z}$. The sum of squared errors may be obtained as

$$SS_E = \mathbf{e}^T \mathbf{e} = [\mathbf{y} - \mathbf{z}]^T [\mathbf{y} - \mathbf{z}] = [\mathbf{y} - \mathbf{X}\theta]^T [\mathbf{y} - \mathbf{X}\theta]. \tag{A5}$$

The minimum of the above may be obtained by finding the location where $d(SS_E)/d\theta = 0$. This operation is given by

$$\frac{d(SS_E)}{d\theta} = 2 \left[\frac{d\mathbf{e}}{d\theta} \right]^T \mathbf{e} = 2\mathbf{X}^T [\mathbf{y} - \mathbf{X}\theta] = 0. \tag{A6}$$

Solving the above for θ yields

$$\hat{\theta} = [\mathbf{X}^T \mathbf{X}]^{-1} [\mathbf{X}^T \mathbf{y}]. \tag{A7}$$

The solution $\hat{\theta}$ provides the simulation model with the parameters that result in the least-square error with respect to the given measurement data. This process is called least-squares method, or linear regression. Generalizing the above process, one may let \mathbf{y} be a $n_y \times 1$ vector of measurement data, θ be a $n_p \times 1$ vector of parameters for the simulation model, with resulting design matrix \mathbf{X} having dimensions of $n_y \times n_p$.

- [1] M. Short, J. J. Quirk, C. Chiquete, and C. D. Meyer, Detonation propagation in a circular arc: reactive burn modelling, *J. Fluid Mech.* **835**, 970 (2018).
- [2] T. L. Jackson and J. Zhang, Density-based kinetics for mesoscale simulations of detonation initiation in energetic materials, *Combust. Theory Modell.* **21**, 749 (2017).
- [3] J. A. Sanchidrián, R. Castedo, L. M. López, P. Segarra, and A. P. Santos, Determination of the JWL constants for ANFO and emulsion explosives from cylinder test data, *Cent. Eur. J. Energ. Mater.* **12**, 177 (2015).
- [4] L. G. Hill and R. A. Catanach, W-76 PBX 9501 Cylinder Tests, Technical Report No. LA-13442-MS, Los Alamos National Laboratory, NM, USA, 1998.
- [5] P. M. Elek, V. V. Džngalašević, S. S. Jaramaz, and D. M. Micković, Determination of detonation products equation of state from cylinder test: Analytical model and numerical analysis, *Therm. Sci.* **19**, 35 (2015).
- [6] P. W. Merchant, S. J. White, and A. M. Collyer, A WBL-consistent JWL equation of state for the HMX-based explosive EDC37 from cylinder tests, in *12th International Detonation Symposium*, August, 2002 (Office of Naval Research, Arlington, 2002).
- [7] W. C. Davis and L. G. Hill, Joints, Cracks, Holes, and Gaps in Detonating Explosives, in *12th International Detonation Symposium* (Office of Naval Research, Arlington, 2002), p. 11.
- [8] M. Short, C. Chiquete, J. B. Bdzil, and J. J. Quirk, Detonation diffraction in a circular arc geometry of the insensitive high explosive PBX 9502, *Combust. Flame* **196**, 129 (2018).
- [9] E. L. Lee and C. M. Tarver, Phenomenological model of shock initiation in heterogeneous explosives, *Phys. Fluids* **23**, 2362 (1980).
- [10] K. Hughes, S. Balachandar, N.-H. Kim, C. Park, R. Haftka, A. Diggs, D. M. Littrell, and J. Darr, Forensic uncertainty quantification for experiments on the explosively driven motion of particles, *J. Verif. Validat. Uncertainty Quantif.* **3**, 041004 (2018).
- [11] K. Hughes, K. Prestridge, N.-H. Kim, R. Haftka, and S. Balachandar, Proton radiography of explosively dispersed metal particles with varying carrier fluid, *WIT Trans. Eng. Sci.* **123**, 223 (2019).
- [12] G. W. Brown, J. A. Tencate, R. DeLuca, P. J. Rae, and S. N. Todd, Dynamic and quasi-static measurements of PBXN-5 and Comp-B explosives, in *Society for Experimental Mechanics—SEM Annual Conference and Exposition on Experimental and Applied Mechanics 2009*, Vol. 2 (SEM, Bethel, 2009), pp. 731–738.
- [13] M. S. Liou, A Sequel to AUSM, Part II: AUSM+—up for all Speeds, *J. Comput. Phys.* **214**, 137 (2006).
- [14] A. Haselbacher, *A WENO Reconstruction Algorithm for Unstructured Grids Based on Explicit Stencil Construction*, AIAA Paper No. 879 (AIAA, Reston, 2005).
- [15] Y. Ling, A. Haselbacher, and S. Balachandar, Transient Phenomena in One-Dimensional Compressible Gas-Particle Flows, *Shock Waves* **19**, 67 (2009).
- [16] Y. Ling, A. Haselbacher, and S. Balachandar, Importance of Unsteady Contributions to Force and Heating for Particles in Compressible Flows. Part 1: Modeling and Analysis for Shock-Particle Interaction, *Int. J. Multiphase Flow* **37**, 1026 (2011).
- [17] Y. Ling, A. Haselbacher, and S. Balachandar, Importance of Unsteady Contributions to Force and Heating for Particles in Compressible Flows. Part 2: Application to Particle Dispersal by Blast Waves, *Int. J. Multiphase Flow* **37**, 1013 (2011).
- [18] H. Jones and A. R. Miller, The Detonation of Solid Explosives: The Equilibrium Conditions in the Detonation Wave-Front and the Adiabatic Expansion of the Products of Detonation, *Proc. R. Soc. Lond. A* **194**, 480 (1948).
- [19] M. L. Wilkins, The Equation of State of PBX 9404 and LXO4-01, Technical Report No. UCRL-7797, Lawrence Livermore Radiation Laboratory, Livermore, 1964.
- [20] E. L. Lee, H. C. Hornig, and J. W. Kury, Adiabatic expansion of high explosive detonation products, Technical Report No. UCRL-50422, Lawrence Livermore Radiation Laboratory, Livermore, 1968.
- [21] B. M. Dobratz, Properties of chemical explosives and explosive simulants, Technical Report No. UCRL-51319; UCRL-51319 (REV. 1), Lawrence Livermore Laboratory, comp. and ed.; California University, Livermore, USA, 1972.
- [22] F. Ouellet, C. Park, B. Rollin, R. T. Haftka, and S. Balachandar, A Kriging surrogate model for computing gas mixture equations of state, *J. Fluids Eng.* **141**, 091301, (2019).

- [23] R. Menikoff, JWL equation of state, Technical Report No. LA-UR-15-29536, Los Alamos National Laboratory (LANL), Los Alamos, NM (United States), 2015.
- [24] T. L. Jackson, A. M. D. Jost, J. Zhang, P. Sridharan, and G. Amadio, Multi-dimensional mesoscale simulations of detonation initiation in energetic materials with density-based kinetics, *Combust. Theory Modell.* **22**, 291 (2018).
- [25] J. B. Bdzil, T. D. Aslam, R. Henninger, and J. J. Quirk, High-Explosives Performance, Los Alamos Sci. **28**, 96 (2003).
- [26] K. W. Thompson, Time Dependent Boundary Conditions for Hyperbolic Systems, *J. Comput. Phys.* **68**, 1 (1987).
- [27] T. J. Poinsot and S. K. Lele, Boundary Conditions for Direct Simulations of Compressible Viscous Flows, *J. Comput. Phys.* **101**, 104 (1992).
- [28] A. Saltelli, M. Ratto, T. Andres, F. Campolongo, J. Cariboni, D. Gatelli, M. Saisana, and S. Tarantola, Global Sensitivity Analysis: The Primer, *Int. Statist. Rev.* **76**, 452 (2008).
- [29] W. Chen, R. Jin, and A. Sudjianto, Analytical Global Sensitivity Analysis and Uncertainty Propagation for Robust Design, *J. Quality Technol.* **38**, 333 (2006).
- [30] S. Bae, N. H. Kim, C. Park, and Z. Kim, Confidence interval of Bayesian Network and Global sensitivity analysis, *AIAA J.* **55**, 3916 (2017).
- [31] D. J. C. MacKay, Introduction to Gaussian processes, NATO ASI Series F Comput. Syst. Sci. **168**, 133 (1998).
- [32] M. Seeger, Gaussian processes for machine learning, *Inter. J. Neural Syst.* **14**, 69 (2004).
- [33] Y. Ling, J. L. Wagner, S. J. Beresh, S. P. Kearney, and S. Balachandar, Interaction of a Planar Shock Wave with a Dense Particle Curtain: Modeling and Experiments, *Phys. Fluids* **24**, 113301 (2012).
- [34] M. Parmar, A. Haselbacher, and S. Balachandar, On the Unsteady Inviscid Force on Cylinders and Spheres in Subcritical Compressible Flow, *Philos. Trans. R. Soc. A* **366**, 2161 (2008).